6-2009

Nondestructive Electromagnetic Material Characterization using a Dual Waveguide Probe: A Full Wave Solution

Milo W. Hyde IV
Air Force Institute of Technology

James W. Stewart

Michael J. Havrilla
Air Force Institute of Technology

William P. Baker
Air Force Institute of Technology

Edward Rothwell

See next page for additional authors

Recommended Citation

Hyde, M. W., Stewart, J. W., Havrilla, M. J., Baker, W. P., Rothwell, E. J., & Nyquist, D. P. (2009). Nondestructive electromagnetic material characterization using a dual waveguide probe: A full wave solution. Radio Science, 44:, RS3013. https://doi.org/10.1029/2008RS003937

Nondestructive electromagnetic material characterization using a dual waveguide probe: A full wave solution

Milo W. Hyde IV,[1] James W. Stewart,[1] Michael J. Havrilla,[1] William P. Baker,[2] Edward J. Rothwell,[3] and Dennis P. Nyquist[3]

Received 12 June 2008; revised 9 February 2009; accepted 30 March 2009; published 20 June 2009.

[1] A nondestructive technique for determining the complex permittivity and permeability of a perfect electric conductor backed magnetic shielding material using a dual waveguide probe is presented. The dual waveguide probe allows for the simultaneous collection of reflection and transmission coefficients which distinguishes it from single probe methods common in the literature. Theoretical development of these coefficients, which is accomplished through a coupled magnetic field integral equations formulation using Love's equivalence principle and solved via the method of moments (MOM), is discussed. Evaluation of the resulting MOM impedance matrix elements is performed using complex plane integration leading to enhanced computational efficiency and physical insight. Comparison of the theoretical and measured reflection and transmission coefficients using a root finding algorithm leads to the desired permittivity and permeability. Measurement results of a magnetic shielding material are presented and compared to traditional methods for the purpose of validating the new technique. The probe's sensitivity to aperture alignment, sample thickness, and flange thickness is also investigated.

Citation: Hyde, M. W., IV, J. W. Stewart, M. J. Havrilla, W. P. Baker, E. J. Rothwell, and D. P. Nyquist (2009), Nondestructive electromagnetic material characterization using a dual waveguide probe: A full wave solution, *Radio Sci.*, *44*, RS3013, doi:10.1029/2008RS003937.

1. Introduction

[2] Rectangular, circular, and coaxial waveguide probes have received much attention in the literature. First mention of their use for near-field measurements dates back 50 years [*Richmond and Tice*, 1955]. More recently, they have been used to nondestructively evaluate various materials. Most notably, *Baker-Jarvis et al.* [1994], *Chang et al.* [1997], and *Li and Chen* [1995] used waveguide probes to nondestructively extract complex permittivity and to some extent permeability from unknown materials, including liquids, soils, and RF shielding materials [*Bois et al.*, 1999; *Cataldo et al.*, 2005; *Maode et al.*, 1999; *Shin and Eom*, 2003; *Stewart and Havrilla*, 2006; *Tantot et al.*, 1997; *Teodoridis et al.*, 1985]. *Mazlumi et al.* [2006], *Huber et al.* [1997], and *Yeh and Zoughi* [1994] developed methods for detecting subsurface cracks in metals and coatings. Last, in one of their more fascinating applications, *Popovic et al.* [2005] and *Bao et al.* [1997] applied open-ended coaxial probes to the measurement of biological tissue: Popovic to breast tissue, Bao to brain tissue. Because of their geometry, waveguide probes are ideal for nondestructive evaluation of materials. Nearly all published research focuses on obtaining the reflection coefficient, using a single probe, from an unknown material backed by a perfect electric conductor (PEC) or a dielectric half-space. While this scenario is well suited for determining complex permittivity of an unknown material, it presents challenges when one also wants to find the complex permeability of a magnetic material. Several authors have developed techniques to fill this shortfall: two thickness method, frequency varying method, and sample added method; however, these techniques are not always applicable [*Baker-Jarvis et al.*, 1994; *Chen et al.*, 2005; *Maode et al.*, 1999; *Stewart and Havrilla*, 2006; *Tantot et al.*, 1997; *Wang et al.*, 1998]. A more suitable alternative would be a waveguide probe system which allows the simultaneous collection of reflection and transmission coefficients since such measurements are

[1]Department of Electrical and Computer Engineering, Air Force Institute of Technology, Wright-Patterson Air Force Base, Ohio, USA.
[2]Department of Mathematics, Air Force Institute of Technology, Wright-Patterson Air Force Base, Ohio, USA.
[3]Department of Electrical and Computer Engineering, Michigan State University, East Lansing, Michigan, USA.

0048-6604/09/2008RS003937

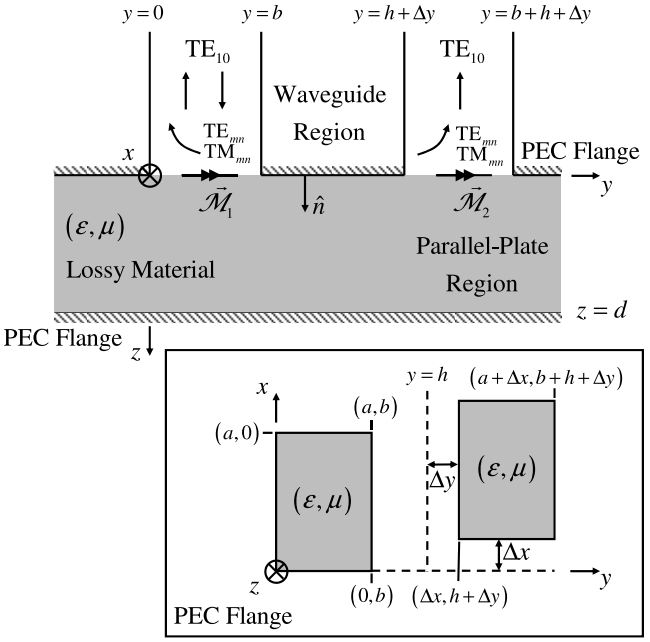

Figure 1. (top) Side and (bottom) top views of the dual waveguide probe measurement geometry.

independent over all wavelengths (thereby avoiding the necessity of using an underdetermined reflection-only optimization algorithm) and are thus the most efficient means of determining both permittivity and permeability. Such a system, referred to as a dual waveguide probe, was presented by *Stewart and Havrilla* [2007]; however, the authors restricted their analysis to only the dominant mode and did not investigate the effects of waveguide misalignment. The purpose of this paper is to extend the dual waveguide probe introduced by *Stewart and Havrilla* [2007] incorporating all modes (full-wave analysis) and investigate the effects of waveguide misalignment. Including these aspects greatly complicates theoretical development and represents a significant contribution to the subject.

[3] In order to fully characterize a magnetic material, i.e., determine complex permittivity and permeability, theoretical expressions for the reflection and transmission coefficients must be found. Figure 1 shows the dual waveguide probe structure analyzed in this paper. The structure consists of two rectangular waveguides attached to an infinite PEC flange. The material under test is assumed to be PEC-backed. Using Love's equivalence principle, the waveguide apertures in Figure 1 can be replaced with equivalent magnetic currents emanating in a parallel-plate environment [*Collin*, 1991; *Peterson et al.*, 1998]. With these currents and the Green's function for a parallel-plate waveguide, one can find an expression for the magnetic field in the parallel-plate region. The magnetic field in the waveguide region can be represented as a sum of TE and TM modes whose amplitude coefficients are related to the equivalent aperture currents. Enforcing the continuity of transverse modal waveguide and parallel-plate magnetic fields at the waveguide apertures produces a system of coupled magnetic field integral equations (MFIEs). Solving this coupled MFIE system using the method of moments (MOM) yields theoretical values for the reflection and transmission coefficients. These theoretical values can then be compared to measured data and the difference minimized via nonlinear least squares or Newton's root finding algorithm to yield complex permittivity and permeability values.

[4] In this paper, the dual waveguide probe structure in Figure 1 is analyzed. Specifically, a lossy magnetic shielding material permanently affixed to a PEC surface is investigated due to its common use in EMC/EMI applications. Included in this analysis is the development of the system of coupled MFIEs along with a discussion of how the resulting MOM spectral domain integrals are evaluated via complex plane analysis. Last, measurement results of a PEC-backed magnetic shielding material are presented comparing the dual waveguide probe measurement system (Figure 1) with traditional destructive waveguide techniques [*Nicolson and Ross*, 1970; *Weir*, 1974]. Included in these measurement results is the

system's sensitivity to probe alignment, sample thickness, and flange thickness.

2. Formulation and Solution of Coupled Magnetic Field Integral Equations

[5] Material characterization requires one to solve forward and inverse problems. The forward problem (the subject of this section) involves finding theoretical expressions for the reflection and transmission coefficients. Since these expressions are functions of permittivity and permeability, an inverse operation is required to extract these parameters. In rare instances direct closed-form expressions can be found that relate permittivity and permeability to reflection and transmission coefficients [*Nicolson and Ross*, 1970; *Weir*, 1974]. However, in most cases (including the one presented in this paper), the inverse problem (discussed in section 4) must be solved using numerical inversion techniques such as Newton's root finding algorithm or nonlinear least squares. It is important to note that since the technique proposed here involves two measurements and two unknowns, the solution algorithm is well posed and consequently avoids the problems of nonuniqueness inherent in underdetermined reflection-only methods.

[6] Consider the measurement geometry shown in Figure 1: two PEC rectangular waveguides of dimensions $a \times b$ are attached to an infinite PEC flange. An incident TE_{10} mode excitation is assumed to exist in probe 1. Probe 2 allows an uncertainty in placement given by Δx and Δy with $h + \Delta y > b$ (probe 2 is not allowed to overlap probe 1) necessary for the sensitivity analysis performed in section 4. The PEC flange structure is placed on a PEC-backed magnetic shielding material of thickness d forming a parallel-plate region. Theoretical expressions for the reflection and transmission coefficients can be found through appropriate boundary condition enforcement on the electric and magnetic fields in the waveguide and parallel-plate regions. In the waveguide regions, the transverse electric and magnetic fields take the form of a superposition of transverse electric (TE) and transverse magnetic (TM) rectangular waveguide modes:

$$\begin{aligned}\vec{E}_t^{(1)} &= \vec{e}_{10}^{(1)} e^{-\gamma_{10} z} + \sum_{m,n} \Gamma_{mn} \vec{e}_{mn}^{(1)} e^{\gamma_{mn} z} \\ \vec{H}_t^{(1)} &= \vec{h}_{10}^{(1)} e^{-\gamma_{10} z} - \sum_{m,n} \Gamma_{mn} \vec{h}_{mn}^{(1)} e^{\gamma_{mn} z}\end{aligned} \tag{1}$$

in probe 1 and

$$\begin{aligned}\vec{E}_t^{(2)} &= \sum_{m,n} \mathrm{T}_{mn} \vec{e}_{mn}^{(2)} e^{\gamma_{mn} z} \\ \vec{H}_t^{(2)} &= -\sum_{m,n} \mathrm{T}_{mn} \vec{h}_{mn}^{(2)} e^{\gamma_{mn} z}\end{aligned} \tag{2}$$

in probe 2 [*Collin*, 1991]. In (1) and (2) for the mn^{th} mode, Γ_{mn} is the reflection coefficient, T_{mn} is the transmission (i.e., coupling) coefficient, γ_{mn} is the propagation constant, and $\vec{e}_{mn}$ and $\vec{h}_{mn}$ are the transverse modal distributions of the electric and magnetic fields, respectively; they are shown in Appendix A. The transverse fields in the parallel-plate region of Figure 1 can be found by replacing the waveguide apertures with magnetic currents $\vec{\mathcal{M}}_1$ and $\vec{\mathcal{M}}_2$ in accordance with Love's equivalence principle [*Collin*, 1991; *Peterson et al.*, 1998]. Making use of the parallel-plate Green's function, the transverse magnetic field can be found from the following expression

$$\vec{H}_t^{pp} = \frac{1}{j\omega\mu\varepsilon}\left(k^2 + \nabla_t \nabla\cdot\right)\vec{F} \tag{3}$$

where the electric vector potential $\vec{F}$ is given by

$$\begin{aligned}\vec{F} = &\int_0^b \int_0^a \overleftrightarrow{G}(x,y,z|x',y',0)\cdot\varepsilon\vec{\mathcal{M}}_1(x',y')dx'dy' \\ &+ \int_{h+\Delta y}^{b+h+\Delta y} \int_{\Delta x}^{a+\Delta x} \overleftrightarrow{G}(x,y,z|x',y',0)\cdot\varepsilon\vec{\mathcal{M}}_2(x',y')dx'dy',\end{aligned} \tag{4}$$

$k = \omega\sqrt{\varepsilon\mu}$ is the complex-valued wave number of the material, and ∇_t is the transverse gradient operator

$$\nabla_t = \hat{x}\frac{\partial}{\partial x} + \hat{y}\frac{\partial}{\partial y}. \tag{5}$$

In (4), $\overleftrightarrow{G}$ is the spectral-domain representation (i.e., rectangular form) of the dyadic, parallel-plate Green's function derived by *Hanson and Yakovlev* [2001]:

$$\begin{aligned}\overleftrightarrow{G} &= \hat{x}G_t\hat{x} + \hat{y}G_t\hat{y} + \hat{z}G_n\hat{z} \\ G_{t,n} &= \frac{1}{(2\pi)^2}\int_{-\infty}^{\infty}\int_{-\infty}^{\infty} g_{t,n}(\xi,\eta;z|z')e^{j\xi(x-x')}e^{j\eta(y-y')}d\xi d\eta \\ g_{t,n} &= \frac{\cosh p(d-|z-z'|) \pm \cosh p(d-(z+z'))}{2p\sinh pd}\end{aligned} \tag{6}$$

where G_t and G_n are the transverse and normal components of the Green's function, respectively, d is the thickness of the material, and $p = \sqrt{\xi^2 + \eta^2 - k^2}$ is the spectral domain, z-directed wave number [*Stewart and Havrilla*, 2006; *Hyde and Havrilla*, 2008]. Note that the equivalent magnetic currents maintain all components of the electric and magnetic fields and explain why both TE and TM modes are required in the rectangular waveguide modal expansions in (1) and (2). With expressions for the

transverse fields in the waveguide and parallel-plate regions, a system of coupled MFIEs can be formed by enforcing the continuity of transverse magnetic fields at the waveguide apertures:

$$\vec{h}_{10}^{(1)} - \sum_{m,n} \Gamma_{mn} \vec{h}_{mn}^{(1)} = \frac{1}{j\omega\mu} \left(k^2 + \nabla_t \nabla \cdot\right) \left[\int_{S_1} \overleftrightarrow{G}\,(z=0|z'=0) \cdot \vec{\mathcal{M}}_1 ds' + \int_{S_2} \overleftrightarrow{G}\,(z=0|z'=0) \cdot \vec{\mathcal{M}}_2 ds' \right] \quad x,y \in S_1 \tag{7}$$

$$- \sum_{m,n} \mathrm{T}_{mn} \vec{h}_{mn}^{(2)} = \frac{1}{j\omega\mu} \left(k^2 + \nabla_t \nabla \cdot\right) \left[\int_{S_1} \overleftrightarrow{G}\,(z=0|z'=0) \cdot \vec{\mathcal{M}}_1 ds' + \int_{S_2} \overleftrightarrow{G}\,(z=0|z'=0) \cdot \vec{\mathcal{M}}_2 ds' \right] \quad x,y \in S_2 \tag{8}$$

where S_1 and S_2 have been introduced to represent the limits of integration in (4). These coupled MFIEs can be solved for the reflection and transmission coefficients using the MOM. The first step in the MOM is to choose suitable basis functions to represent the unknown equivalent currents, $\mathcal{M}_1$ and $\mathcal{M}_2$ in this instance. To ensure fast convergence, basis functions should be chosen which closely resemble the physical distribution of the current they are representing. In the case of magnetic currents,

$$\vec{\mathcal{M}} = -\hat{n} \times \vec{E}, \tag{9}$$

where $\hat{n} = \hat{z}$ is the unit-normal vector to the surface on which the current exists as shown in Figure 1. It is for this reason and to enforce continuity of the transverse electric field in the original problem that the transverse electric field distributions in (1) and (2) were chosen as a basis set for $\vec{\mathcal{M}}_1$ and $\vec{\mathcal{M}}_2$, namely

$$\begin{aligned} \vec{\mathcal{M}}_1 &= -\hat{z} \times \left[\vec{e}_{10}^{(1)} + \sum_{m,n} \Gamma_{mn} \vec{e}_{mn}^{(1)} \right] \\ \vec{\mathcal{M}}_2 &= -\hat{z} \times \left[\sum_{m,n} \mathrm{T}_{mn} \vec{e}_{mn}^{(2)} \right]. \end{aligned} \tag{10}$$

[7] Substituting (10) into (7) and (8) results in a system of 2 equations and 2N unknowns. In order to establish a full rank matrix equation, testing functions must be chosen and applied to (7) and (8). In this analysis, the transverse magnetic field distributions, $\vec{h}_{\tilde{m}\tilde{n}}^{(1)}$ and $\vec{h}_{\tilde{m}\tilde{n}}^{(2)}$, were chosen as testing functions to take advantage of the orthogonality of waveguide modes. Applying these testing functions to (7) and (8) via the inner product produces a 2N by 2N matrix equation $\mathbf{Ax} = \mathbf{b}$, where $\mathbf{A}$ is the impedance matrix, $\mathbf{x}$ is a vector containing the unknown reflection and transmission coefficients, and $\mathbf{b}$ is a vector containing the incident field excitation. Physical insight can be gleaned by inspection of $\mathbf{A}$:

$$\mathbf{A} = \begin{bmatrix} \mathbf{A}^{11} & \mathbf{A}^{12} \\ \mathbf{A}^{21} & \mathbf{A}^{22} \end{bmatrix} = \begin{bmatrix} a_{10,10}^{11} & \cdots & a_{10,mn}^{11} & a_{10,10}^{12} & \cdots & a_{10,mn}^{12} \\ \vdots & \ddots & \vdots & \vdots & \ddots & \vdots \\ a_{\tilde{m}\tilde{n},10}^{11} & \cdots & a_{\tilde{m}\tilde{n},mn}^{11} & a_{\tilde{m}\tilde{n},10}^{12} & \cdots & a_{\tilde{m}\tilde{n},mn}^{12} \\ a_{10,10}^{21} & \cdots & a_{10,mn}^{21} & a_{10,10}^{22} & \cdots & a_{10,mn}^{22} \\ \vdots & \ddots & \vdots & \vdots & \ddots & \vdots \\ a_{\tilde{m}\tilde{n},10}^{21} & \cdots & a_{\tilde{m}\tilde{n},mn}^{21} & a_{\tilde{m}\tilde{n},10}^{22} & \cdots & a_{\tilde{m}\tilde{n},mn}^{22} \end{bmatrix} \tag{11}$$

where the submatrix $\mathbf{A}^{ij}$ (for $i, j = 1,2$) represents how a source in probe j influences the field in probe i. Thus, $\mathbf{A}^{11}$ and $\mathbf{A}^{22}$ are self-interaction terms within each probe; whereas, $\mathbf{A}^{12}$ and $\mathbf{A}^{21}$ represent cross-coupling effects between the probes. As expected by reciprocity, it is found that $\mathbf{A}^{12}$ and $\mathbf{A}^{21}$ are equivalent. It is also found that $\mathbf{A}^{11}$ and $\mathbf{A}^{22}$ are equal due to the symmetry of the geometry. The subscript of each matrix element describes how a certain waveguide mode couples into another. For example, the $\tilde{m}\tilde{n},mn$ elements describe how the mn^{th} source mode couples into the $\tilde{m}\tilde{n}^{\text{th}}$ field mode.

3. Spectral Domain Integration

[8] In the previous section, a system of coupled MFIEs is derived. Solving this system via the MOM leads to a matrix equation $\mathbf{Ax} = \mathbf{b}$, where $\mathbf{A}$ is the impedance matrix, $\mathbf{x}$ is a vector containing the unknown reflection and transmission coefficients, and $\mathbf{b}$ is a vector containing the incident field excitation. Whereas in the last section, $\mathbf{A}$ is inspected macroscopically, the purpose of this section is to investigate $\mathbf{A}$ microscopically, i.e., investigate the individual elements of $\mathbf{A}$. This section discusses the benefits of using the spectral domain (i.e.,

rectangular) form of the Green's function expressed in (6) for evaluating the elements of **A** via complex plane integration. Also discussed later in this section is the insight gained from using the spatial (i.e., polar) form of the Green's function derived from (6).

[9] While it is possible to find the elements of **A** using numerical integration and the spatial form of the Green's function, physical insight and efficient computation can be obtained by evaluating the elements of **A** using the spectral-domain representation of the Green's function given in (6). If one were to evaluate the elements of **A** in the spatial domain, four integrals would have to be evaluated numerically: two testing integrals and two basis integrals involving strongly singular integrands. On the other hand, evaluating the elements of **A** using the spectral-domain representation of the Green's function permits all spatial integrals (both testing and basis integrals) and one of the spectral integrals to be performed in closed form. This results in expressions for the elements of **A** involving a rapidly converging infinite series and an infinite integral which can easily be computed numerically. As an example, the calculation of the $a^{12}_{\tilde{m}0,m0}$ elements of **A** are shown. This set of elements provides an excellent example of the role probe alignment uncertainty plays in the analysis. The remaining elements of **A** can be evaluated in a similar manner. The impedance matrix elements $a^{12}_{\tilde{m}0,m0}$ have the following form

$$a^{12}_{\tilde{m}0,m0} = \frac{m\pi/a}{j\omega\mu(2\pi)^2}\int_{-\infty}^{\infty}\int_{-\infty}^{\infty}\frac{\cosh pd}{p\sinh pd}\left(k^2-\xi^2\right) \cdot f_{\tilde{m}0}(\xi,\eta)g_{m0}(\xi,\eta)d\eta d\xi \tag{12}$$

where

$$f_{\tilde{m}0} = \int_0^a \sin\left(\frac{\tilde{m}\pi x}{a}\right)e^{j\xi x}dx\int_0^b e^{j\eta y}dy$$
$$g_{m0} = \int_{\Delta x}^{a+\Delta x}\sin\left[\frac{m\pi}{a}(x'-\Delta x)\right]e^{-j\xi x'}dx'\int_{h+\Delta y}^{b+h+\Delta y}e^{-j\eta y'}dy' \tag{13}$$

As previously mentioned, the spatial integrals in (13) can be evaluated in closed form. Substituting the results of (13) into (12) produces

$$a^{12}_{\tilde{m}0,m0} = \frac{\tilde{m}m^2\pi^3/a^3}{j\omega\mu(2\pi)^2}\int_{-\infty}^{\infty}\left(k^2-\xi^2\right)\frac{\left(1+(-1)^{m+1}e^{-j\xi a}\right)\left(1+(-1)^{\tilde{m}+1}e^{j\xi a}\right)e^{-j\xi\Delta x}}{\left(\xi^2-(m\pi/a)^2\right)\left(\xi^2-(\tilde{m}\pi/a)^2\right)}\cdot \int_{-\infty}^{\infty}\frac{\cosh pd}{p\sinh pd}\frac{\left(1-e^{-j\eta b}\right)\left(1-e^{j\eta b}\right)}{\eta^2}e^{-j\eta(h+\Delta y)}d\eta d\xi \tag{14}$$

Note that the η integrand in (14) has simple poles, corresponding to parallel-plate modes at $\eta = \pm\sqrt{k^2-\xi^2-(\ell\pi/d)^2}$ (for ℓ = 0, 1, 2, ...) due to the *p*sinh *pd* term and a removable double pole at $\eta = 0$ resulting from the *y*-invariant, TE_{10} rectangular waveguide mode. Since (14) represents the coupling that occurs between apertures 1 and 2, it is reasonable that the double pole at $\eta = 0$, a product of the incident field, is removable. Note that this apparent double pole becomes a simple pole for the self elements of the impedance matrix because of the direct interaction these terms have with the TE_{10} incident field. In addition to simple poles, the η integrand of (14) also has branch points at $\eta = \pm\sqrt{k^2-\xi^2}$, which along with the associated branch cut contributions, are removable because the integrand is even in *p* [*Stewart and Havrilla*, 2006; *Hyde and Havrilla*, 2008]. This result makes physical sense when one considers that the structure in Figure 1 is closed and consequently nonradiating. Since the branch points and branch cuts in the η integrand are removable, the η integral contains only parallel-plate pole singularities and can therefore be evaluated using Cauchy's integral theorem. With the condition that $h + \Delta y > b$ (postulated earlier), the η integral in (14) requires lower half plane closure to converge. Figure 2 shows the complex η plane with the appropriately deformed contour. By utilizing both Cauchy's integral theorem and formula and Jordan's lemma [*Kwok*, 2002], the η integral in (14) evaluates to

$$\int_{-\infty}^{\infty}\frac{\cosh pd}{p\sinh pd}\frac{\left(1-e^{-j\eta b}\right)\left(1-e^{j\eta b}\right)}{\eta^2}e^{-j\eta(h+\Delta y)}d\eta = -\frac{j2\pi}{d}\sum_{\ell=0}^{\infty}\frac{\left(1-e^{-j\eta_\ell b}\right)\left(1-e^{j\eta_\ell b}\right)e^{-j\eta_\ell(h+\Delta y)}}{\eta_\ell^3\left(1+\delta_{\ell,0}\right)} \tag{15}$$
$$\eta_\ell = \sqrt{k^2-\xi^2-(\ell\pi/d)^2},\ \delta_{\ell,0} = \begin{cases}1 & \ell = 0\\ 0 & \ell \neq 0\end{cases}$$

This pole series representation is very rapidly converging (a factor of ten faster than an adaptive quadrature routine in computation time) due to reduced numerical operations, the exponential decay terms, and the η_ℓ^3 behavior in the denominator. Note that the simple poles η_ℓ become branch points in the ξ plane resulting in irremovable and relatively complicated branch cut contributions (i.e., continuous spectrum representation required to model cylindrically outgoing waves due to discretization of the η integral) [*Stewart and Havrilla*, 2006; *Hyde and Havrilla*, 2008]. It is for this reason that the remaining ξ integral in (14) is calculated numerically using real axis adaptive quadrature instead of Cauchy's integral theorem.

[10] While the analysis of the preceding paragraph utilized the spectral domain (i.e., rectangular) form of the Green's function for numerical implementation and

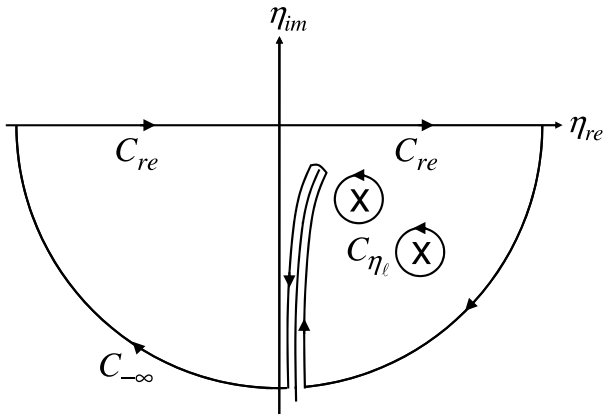

Figure 2. Lower half complex η plane (branch point and associated branch cut are removable).

physical insight, the spatial (i.e., polar) form provides a key piece of additional insight which is imperative for dual waveguide probe design. The polar form is readily identified by first substituting $x - x' = R\cos\theta$, $y - y' = R\sin\theta$, $\xi = \lambda\cos\phi$, and $\eta = \lambda\sin\phi$ into (6) resulting in

$$G_{t,n} = \frac{1}{(2\pi)^2}\int_0^\infty \lambda g_{t,n}(\lambda; z|z') \int_{-\pi}^{\pi} e^{j\lambda R\cos(\phi-\theta)} d\phi d\lambda, \quad (16)$$

where $\lambda = \sqrt{\xi^2 + \eta^2}$, $R = |\vec{\rho} - \vec{\rho}'|$ is the distance between the source and observation point, and $g_{t,n}$ is defined in (6) with $p = \sqrt{\lambda^2 - k^2}$. The integral with respect to ϕ is well known and readily found to be $2\pi J_0(\lambda R)$. Using the Bessel-Hankel function relation and the analytic continuation formula,

$$\begin{aligned} J_0(z) &= \frac{1}{2}\left[H_0^{(1)}(z) + H_0^{(2)}(z)\right] \\ H_0^{(2)}(z) &= -H_0^{(1)}(-z) \end{aligned}, \quad (17)$$

respectively, (16) can be cast into the form

$$G_{t,n} = \frac{1}{4\pi}\int_{-\infty}^{\infty} \lambda g_{t,n}(\lambda; z|z') H_0^{(2)}(\lambda R) d\lambda. \quad (18)$$

Examination of $g_{t,n}$ reveals that the integrand in (18) is even in $p = \sqrt{\lambda^2 - k^2}$. Thus, the branch points $\lambda = \pm k$ and associated branch cut contributions are removable as physically expected for this closed structure. Only parallel-plate mode poles exist at $\lambda_\ell = \sqrt{k^2 - (\ell\pi/d)^2}$ (for $\ell = 0, 1, 2, \ldots$) due to the *p*sinh *pd* term. Since the Hankel function of the second kind behaves asymptotically like

$$H_0^{(2)}(\lambda R) \sim \sqrt{\frac{j2}{\pi\lambda R}} e^{-j\lambda R}, \quad (19)$$

lower half λ plane closure is required for convergence. Applying Cauchy's integral theorem to (18) produces the desired spatial (i.e., polar) form

$$\begin{aligned} G_{t,n} = {} & \frac{-j}{4d\left(1 + \delta_{\ell,0}\right)} H_0^{(2)}(\lambda_\ell R) \\ & \cdot \left[\cos\left(\frac{\ell\pi}{d}|z - z'|\right) \pm \cos\left(\frac{\ell\pi}{d}(z + z')\right)\right] \end{aligned} \quad (20)$$

where $\delta_{\ell,0}$ is defined in (15). This result makes physical sense, as one would expect the field in the parallel-plate region to possess a standing wave behavior in the z direction and cylindrical wave behavior in the radial direction. The key insight from (20) is that the $\ell = 0$ dominant mode (a TE^ρ mode) has a propagation constant equal to $\lambda_0 = k$ and therefore has an asymptotic radial field behavior proportional to e^{-jkR}. This simple result is important for design purposes as it allows easy calculation of the expected attenuation of a given lossy shielding material and thus provides practical guidance on how large flange dimensions must be to accommodate the infinite flange assumption. This concept is developed further in section 4.

4. Results

[11] In this section, dual waveguide probe measurement results are compared to traditional destructive waveguide techniques such as those developed by Nicolson, Ross, and Weir (NRW) [*Nicolson and Ross*, 1970; *Weir*, 1974]. The material measured in this experiment is Emerson and Cuming ECCOSORB® FGM-125. This material is a lossy, silicon based, magnetic shielding material approximately 0.3175 cm (0.125 in.) thick. Figure 3 shows a photograph of the dual waveguide probe used in this experiment, including the PEC-backed shielding material. The dual probe measurement apparatus consists of two X band rectangular waveguides connected with screws to a 30.48 cm × 30.48 cm × 0.9525 cm (12 in. × 12 in. × 0.375 in.) aluminum flange plate. Because of the lossy nature of the material under

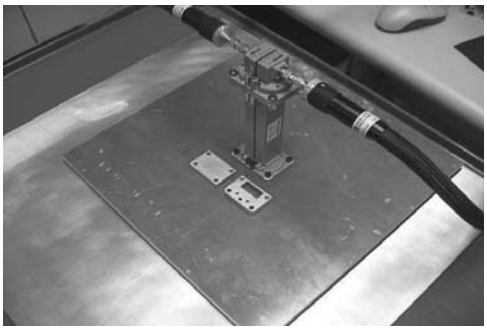

Figure 3. Photograph of the dual waveguide probe including machined, precision line standard and short.

test, the waveguides are machined so that only a 0.381 cm (0.150 in.) spacing exists between their apertures to ensure sufficient coupling. The apparatus is calibrated using a thru-reflect-line (TRL) calibration [*Engen and Hoer*, 1979]. Measurement of the complex reflection and transmission coefficients is performed using an Agilent Technologies E8362B vector network analyzer (VNA). Complex permittivity ε_r and permeability μ_r values for FGM-125 are found by solving the following system of equations,

$$\begin{gathered}\left|S_{11}^{thy}(\varepsilon_r,\mu_r)-S_{11}^{meas}\right|\le\delta\\ \left|S_{12}^{thy}(\varepsilon_r,\mu_r)-S_{12}^{meas}\right|\le\delta\\ \left|S_{21}^{thy}(\varepsilon_r,\mu_r)-S_{21}^{meas}\right|\le\delta\\ \left|S_{22}^{thy}(\varepsilon_r,\mu_r)-S_{22}^{meas}\right|\le\delta\\ S_{11}^{thy}=S_{22}^{thy}=\Gamma_{10}\ ,\ S_{12}^{thy}=S_{21}^{thy}=\mathrm{T}_{10}\end{gathered}\quad , \tag{21}$$

at each frequency within specified tolerance δ (typically 10^{-6}) using Gauss-Newton nonlinear least squares.

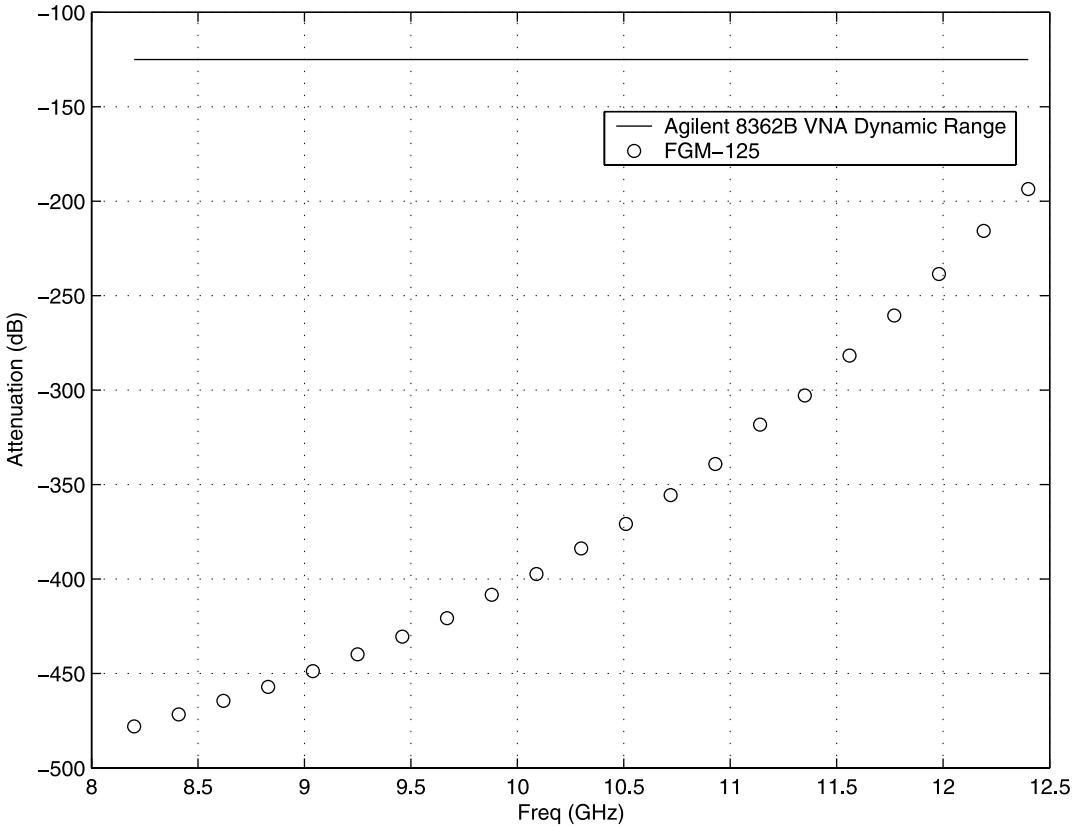

Figure 4. Attenuation of field amplitude propagating to and from the edges of a 30.48 cm × 30.48 cm (12 in. × 12 in.) PEC flange filled with FGM-125. Permittivity and permeability values for FGM-125 used to generate Figure 4 were obtained from the manufacturer.

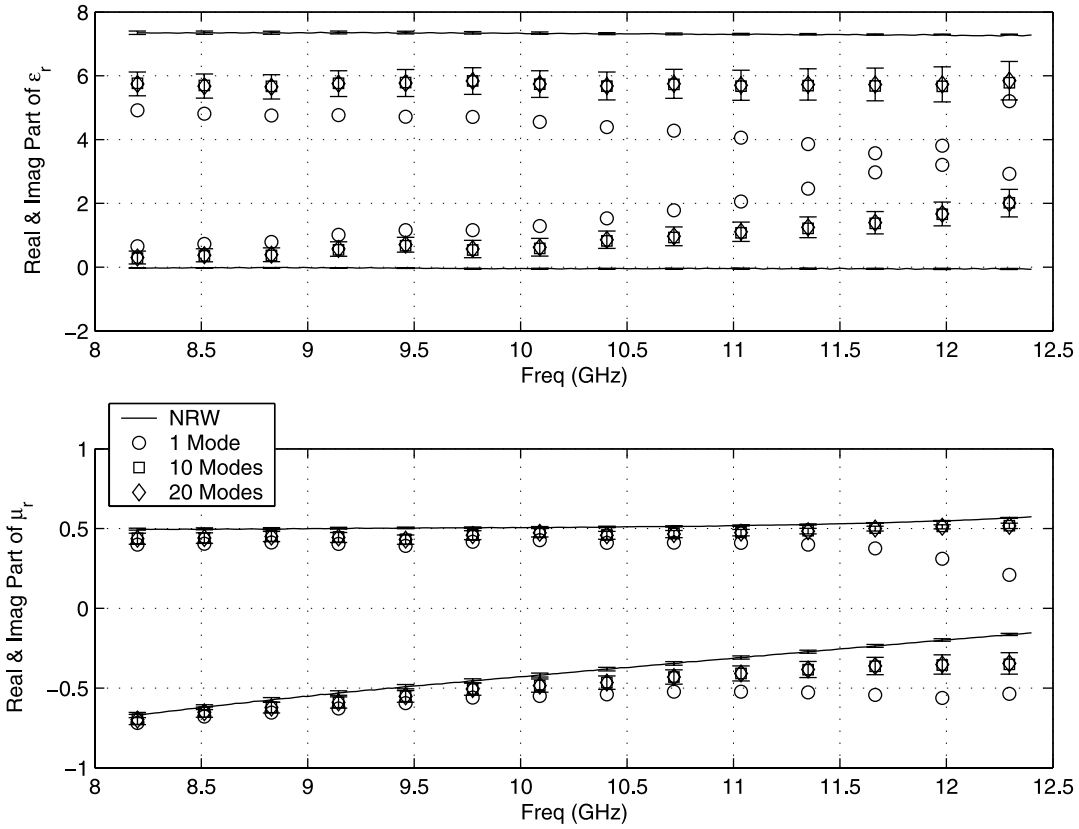

Figure 5. Complex permittivity and permeability results for FGM-125 comparing data obtained from the dual waveguide probe with that obtained from traditional waveguide techniques (NRW). Real and imaginary parts are in the top and bottom part of each plot, respectively. The 1 mode trace incorporates the dominant mode only; whereas, the 10 and 20 modes traces incorporate the first 10 and 20 rectangular waveguide modes, respectively, in order of cutoff frequency.

[12] While the theory presented in the previous two sections can accommodate any material, in practice only sufficiently lossy materials should be measured with the dual waveguide probe. This is because the infinite flange assumed in the theory is not physically realizable. If the cross-sectional dimensions of the flange are not large enough, or the material lossy enough, then it is possible to introduce measurement error from detecting waves reflected from the edges of the flange (henceforth referred to as two-way reflection error). As discussed in the previous section, dominant mode propagation in the parallel-plate region of Figure 1 asymptotically behaves like $H_0^{(2)}(kR) \sim e^{-jkR}$. This simple relation is important for dual waveguide probe design because it allows one to easily determine the approximate field strength at any distance R from the apertures of the probe. With this information and the dynamic range of the VNA, one can calculate the cross-sectional dimensions of the flange so as to ensure negligible two-way reflection error. Figure 4 shows the two-way attenuation of parallel-plate region fields for FGM-125 using the values for permittivity and permeability supplied by the manufacturer. The dynamic range of the Agilent Technologies E8362B is listed at 125 dB [*Agilent Technologies*, 2007]. Figure 4 clearly shows that a 30.48 cm $\times$ 30.48 cm (12 in. $\times$ 12 in.) flange is more than sufficient to ensure negligible two-way reflection error for FGM-125, thus adhering to the infinite flange assumption from a practical implementation viewpoint.

[13] Complex permittivity and permeability results for FGM-125 are shown in Figure 5. Figure 5 compares data obtained from the dual waveguide probe with that obtained from traditional destructive waveguide techniques [*Nicolson and Ross*, 1970; *Weir*, 1974]. The error

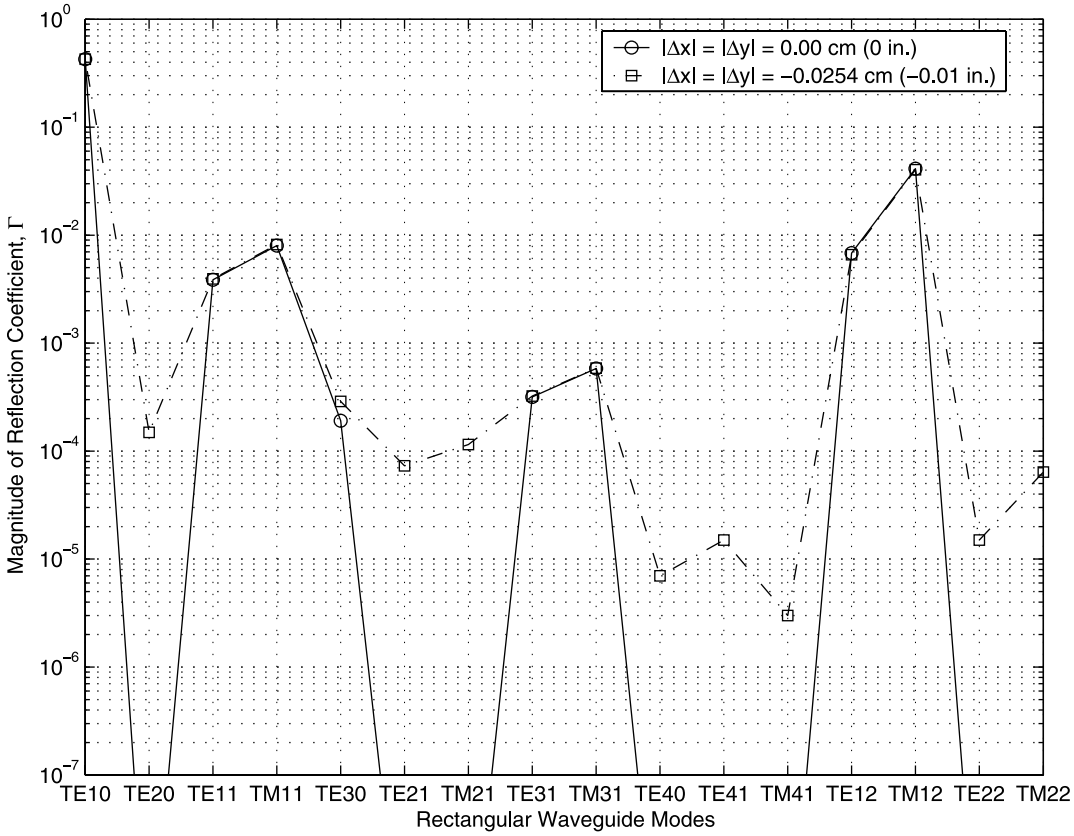

Figure 6. Magnitudes of the first 10 modal reflection coefficients for FGM-125 at 10 GHz comparing aligned and misaligned probe scenarios. When the probes are perfectly aligned, the TE and TM modes of even *m* index are identically zero and hence do not appear on the log-scale plot. TE and TM modes of the same index count as one mode.

bars on the NRW trace represent a combined ±0.0127 cm (±0.005 in.) calibration plane uncertainty and a ±0.0508 mm (±0.002 in.) material thickness uncertainty. The error bars on the 20 modes trace represent a combined ±0.0762 mm (±0.003 in.) flange thickness uncertainty, a ±0.0254 cm (±0.01 in.) probe alignment uncertainty, and a ±0.0508 mm (±0.002 in.) material thickness uncertainty. In order to not clutter Figure 5, no error bars are shown on the 1 and 10 modes traces. Figure 5 shows that the dual waveguide probe measures permittivity with approximately a 10% discrepancy and permeability with less than a 2% discrepancy, relative to the traditional technique data, for most of the frequency band. This higher permittivity discrepancy, especially evident in the nonphysical, positive results for the imaginary part of permittivity, arises from modal expansion choice, the specific geometry of the dual waveguide probe, and the dominant TE_{10} rectangular waveguide mode distribution. Since the material under test is electrically thin and the transverse electric field in the parallel-plate region of Figure 1 is forced to be zero at the PEC boundaries, only a small interrogating electric field exists in the parallel-plate region to measure permittivity. This, however, is not the case for the magnetic field. The transverse magnetic field at the PEC boundaries in the parallel-plate region of Figure 1 is related to the induced electric current on those boundaries and is therefore not zero (in fact, the transverse magnetic field is a maximum at the PEC boundaries). It is for this reason that the dual waveguide probe more accurately measures permeability than permittivity. Similar errors in permittivity measurements, for like measurement geometries, are noted by *Wang et al.* [1998], *Chen et al.* [2005], *Stewart and Havrilla* [2006], *Maode et al.* [1999], *Tantot et al.* [1997], *Li and Chen* [1995], and *Courtney and Motil* [1999]. Several of the researchers state the difficulty of obtaining accurate dielectric loss values (even physically realizable results) for low dielec-

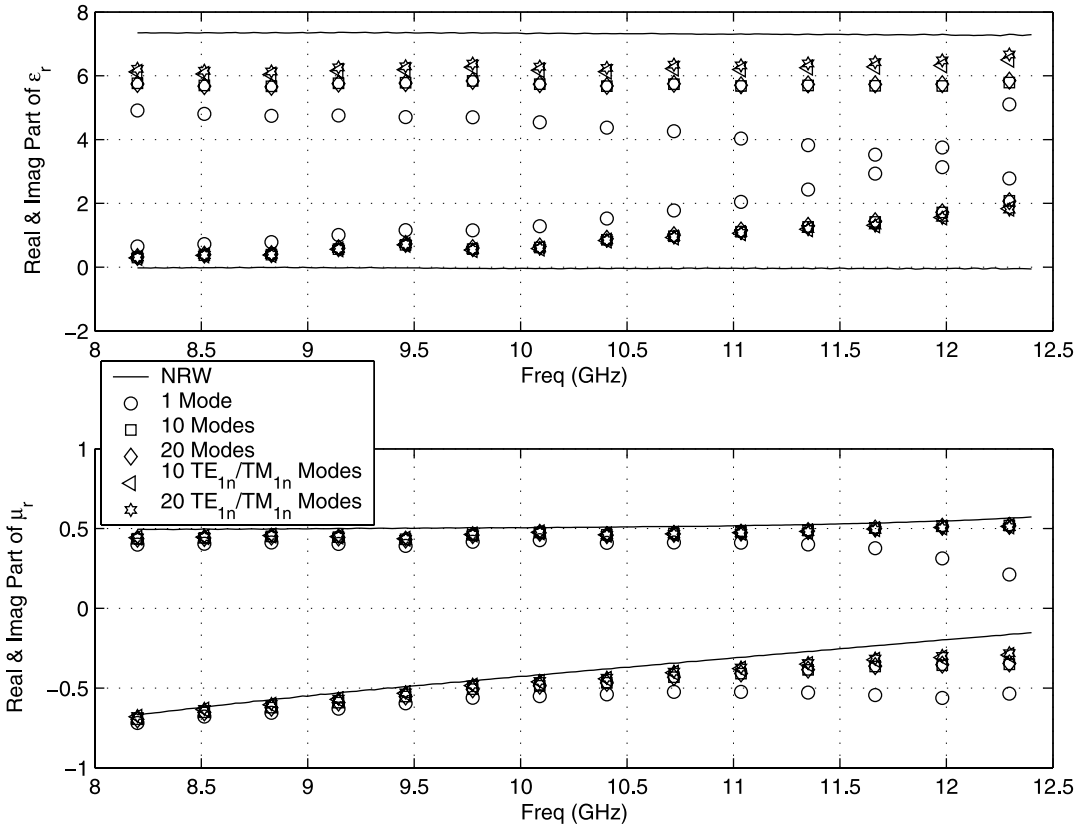

Figure 7. Complex permittivity and permeability results for FGM-125 comparing data obtained from the dual waveguide probe with that obtained from traditional waveguide techniques (NRW). Real and imaginary parts are in the top and bottom part of each plot, respectively. The NRW, 1 mode, 10 modes, and 20 modes traces are identical to those in Figure 5. The 10 and 20 modes TE_{1n}/TM_{1n} traces incorporate the first 10 and 20 TE_{1n}/TM_{1n} rectangular waveguide modes, i.e., n = 0, 1, . . ., 19. Judicious choice of modes has a significant impact on accuracy.

tric loss materials. Of particular note, *Tantot et al.* [1997] report percent errors in the hundreds for dielectric loss measurements. Difficulty with the measurement of dielectric loss is also noted by *Challa et al.* [2008] even when using a standard, transmission/reflection, waveguide geometry. Although their results for dielectric loss are physically realizable, they do note a larger variation of results for the imaginary part of permittivity than for the real part. They also report a 25% discrepancy in dielectric loss values obtained by five different extraction methods. Although the dielectric loss results in Figure 5 are physically unrealizable, they are within the range of dielectric loss results in the literature for PEC-backed measurement scenarios. Even with the permittivity discrepancy in Figure 5, including 10 modes in the theoretical development greatly improves the results when compared to the single mode case. Also note that the inclusion of 20 modes (when ranked according to cutoff) demonstrates that convergence to within a few decimal places is achieved after only approximately 10 modes.

[14] Figure 6 shows the magnitudes of the first 10 modal reflection coefficients for FGM-125 at 10 GHz. Note that the TE_{10} mode is the dominant contributor to the reflection coefficient (as expected due to the TE_{10} mode incident excitation); however, the TE_{11}/TM_{11} and TE_{12}/TM_{12} mode pairs are still significant. These modes are the reason for the substantial improvement in the 10 mode results. Another important physical result is that when the probes are assumed to be perfectly aligned, TE and TM modes of even m index are zero. This result is due to the symmetry of the TE_{10} incident field and the dual waveguide probe geometry. If one can tolerate the probe alignment uncertainty, only odd m index modes need to be included in the theoretical development. As an example, Figure 7 shows the complex permittivity and permeability results for FGM-125 when the first 10 and

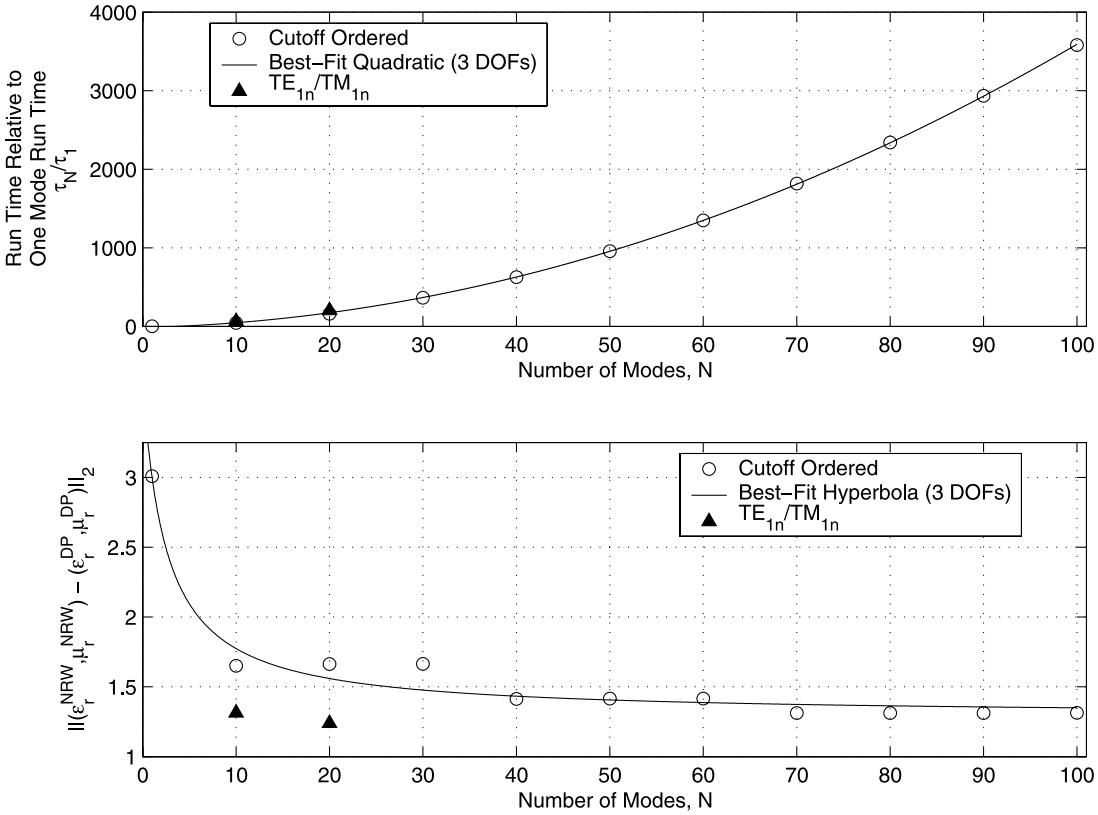

Figure 8. (top) Run time relative to one mode and (bottom) error versus the number of modes, N. Run time increases quadratically with N; whereas, error decreases in a hyperbolic manner. Note, judicious modal expansion choice offers both significant reductions in run time and error.

20 TE_{1n}/TM_{1n} mode pairs, i.e., n = 0, 1,. . ., 19, are considered in the theoretical development. For ease of comparison, the NRW, 1 mode, 10 modes, and 20 modes traces from Figure 5 are included on Figure 7. Calibration plane, probe alignment, material thickness, and flange thickness uncertainties are not taken into account. Note that just including the first 10 TE_{1n}/TM_{1n} mode pairs improves permittivity results by approximately 10% with no subsequent increase in run time over the original, cutoff ordered, 10 modes trace. Thus, a judicious choice of modes (prompted by physical insight) can have a big impact on material extraction accuracy as well as run time. Note, it is again seen from the 20 TE_{1n}/TM_{1n} modes trace that convergence to within a few decimal places is achieved after only approximately 10 modes. Although further enhancement of convergence can be achieved by including more modes, the drawback is that computation time increases quadratically with mode number (demonstrated in Figure 8). Note, although other materials were measured in this investigation, they are not included for the sake of brevity since the results shared similar trends to the data presented here.

5. Conclusion

[15] In this paper, a nondestructive technique for simultaneously determining complex permittivity and permeability of an unknown lossy shielding material permanently affixed to a PEC using a dual waveguide probe is presented. A system of coupled MFIEs is derived by replacing the probe apertures in Figure 1 with equivalent magnetic currents in accordance with Love's equivalence principle. Solving this system of coupled MFIEs using the MOM leads to a matrix equation in terms of unknown modal reflection and transmission coefficients. The complex permittivity and permeability of the unknown material is then found by minimizing the difference between the theoretical and measured coefficients via nonlinear least squares. Also included in the development is a discussion of the

elements forming the MOM impedance matrix. It is shown, upon using the rectangular form of the Green's function, that all spatial integrals can be evaluated in closed form and one of the spectral integrals can be represented as a rapidly converging series using complex plane integration thereby greatly increasing numerical efficiency. In addition, important physical insight and design guidance are gained through the development of the polar form of the Green's function. Last, experimental results of the dual waveguide probe are compared to traditional destructive waveguide methods [*Nicolson and Ross*, 1970; *Weir*, 1974] for the purpose of validating the new technique.

[16] The main contribution of the work presented in this paper, over existing single probe techniques, is that it allows for the simultaneous measurement of reflection and transmission coefficients. Since these measurements are independent over all wavelengths and are observed simultaneously, no underdetermined optimization routines or additional measurements are required to extract permittivity and permeability [*Baker-Jarvis et al.*, 1994; *Chen et al.*, 2005; *Maode et al.*, 1999; *Stewart and Havrilla*, 2006; *Tantot et al.*, 1997; *Wang et al.*, 1998]. The work presented in this paper also significantly extends that presented by *Stewart and Havrilla* [2007] by incorporating higher-order modes and probe alignment uncertainty. The work also investigated the benefits of judicious choice of modal expansion terms. Incorporating these aspects greatly complicates the theoretical development but dramatically improves the material extraction results. The dual waveguide probe's most promising application is in the field of nondestructive inspection. Like the single probe, the dual waveguide probe can also be extended to non-PEC-backed material characterization, subsurface crack detection, in vivo measurement of biological tissue, and measurement of liquids.

Appendix A

[17] The rectangular waveguide transverse electric, $\vec{e}_{mn}$, and magnetic, $\vec{h}_{mn}$, field distributions are

$$\begin{bmatrix} \vec{e}_{mn}^{(1)\mathrm{TE}} \\ \vec{e}_{mn}^{(1)\mathrm{TM}} \end{bmatrix} = \hat{x}\begin{bmatrix} k_y \\ k_x \end{bmatrix}\cos(k_x x)\sin(k_y y) + \hat{y}\begin{bmatrix} -k_x \\ k_y \end{bmatrix}\sin(k_x x)\cos(k_y y)$$
$$\begin{bmatrix} \vec{h}_{mn}^{(1)\mathrm{TE}} \\ \vec{h}_{mn}^{(1)\mathrm{TM}} \end{bmatrix} = \hat{z}\times\begin{bmatrix} \vec{e}_{mn}^{(1)\mathrm{TE}}/\mathrm{Z}_{mn}^{\mathrm{TE}} \\ \vec{e}_{mn}^{(1)\mathrm{TM}}/\mathrm{Z}_{mn}^{\mathrm{TM}} \end{bmatrix} \tag{A1}$$

in probe 1 and

$$\begin{bmatrix} \vec{e}_{mn}^{(2)\mathrm{TE}} \\ \vec{e}_{mn}^{(2)\mathrm{TM}} \end{bmatrix} = \hat{x}\begin{bmatrix} k_y \\ k_x \end{bmatrix}\cos[k_x(x-\Delta x)]\sin[k_y(y-h-\Delta y)] + \hat{y}\begin{bmatrix} -k_x \\ k_y \end{bmatrix}\sin[k_x(x-\Delta x)]\cos[k_y(y-h-\Delta y)]$$
$$\begin{bmatrix} \vec{h}_{mn}^{(2)\mathrm{TE}} \\ \vec{h}_{mn}^{(2)\mathrm{TM}} \end{bmatrix} = \hat{z}\times\begin{bmatrix} \vec{e}_{mn}^{(2)\mathrm{TE}}/\mathrm{Z}_{mn}^{\mathrm{TE}} \\ \vec{e}_{mn}^{(2)\mathrm{TM}}/\mathrm{Z}_{mn}^{\mathrm{TM}} \end{bmatrix} \tag{A2}$$

in probe 2. Here,

$$k_x = \frac{m\pi}{a},\ k_y = \frac{n\pi}{b},\ \gamma_{mn} = \sqrt{k_x^2 + k_y^2 - k_0^2}$$
$$\mathrm{Z}_{mn}^{\mathrm{TE}} = \frac{j\omega\mu_0}{\gamma_{mn}},\ \mathrm{Z}_{mn}^{\mathrm{TM}} = \frac{\gamma_{mn}}{j\omega\varepsilon_0} \tag{A3}$$

References

Agilent Technologies (2007), Agilent PNA microwave network analyzers data sheet, Santa Clara, Calif.

Baker-Jarvis, J., M. D. Janezic, P. D. Domich, and R. G. Geyer (1994), Analysis of an open-ended coaxial probe with lift-off for nondestructive testing, *IEEE Trans. Instrum. Meas.*, *43*(5), 711–718, doi:10.1109/19.328897.

Bao, J., S. Lu, and W. D. Hurt (1997), Complex dielectric measurements and analysis of brain tissues in the radio and microwave frequencies, *IEEE Trans. Microwave Theory Tech.*, *45*(10), 1730–1741, doi:10.1109/22.641720.

Bois, K. J., A. D. Benally, and R. Zoughi (1999), Multimode solution for the reflection properties of an open-ended rectangular waveguide radiating into a dielectric half-space: The forward and inverse problems, *IEEE Trans. Instrum. Meas.*, *48*(6), 1131–1140, doi:10.1109/19.816127.

Cataldo, A., L. Tarricone, A. Trotta, F. Attivissimo, and C. Urso (2005), Time domain reflectometry technique for monitoring of liquid characteristics, in *Proceedings of Instrumentation and Measurement Technology Conference, Ottawa, Canada, 17–19 May*, IEEE Press, Piscataway, N. J.

Challa, R. K., D. Kajfez, J. R. Gladden, A. Z. Elsherbeni, and V. Demir (2008), Permittivity measurement with a non-standard waveguide by using TRL calibration and fractional linear data fitting, *Prog. Electromagn. Res. B*, *2*, 1–13, doi:10.2528/PIERB07102001.

Chang, C., K. Chen, and J. Qian (1997), Nondestructive determination of electromagnetic parameters of dielectric materials at X-band frequencies using a waveguide probe system, *IEEE Trans. Instrum. Meas.*, *46*(5), 1084–1092, doi:10.1109/19.676717.

Chen, C., Z. Ma, T. Anada, and J. Hsu (2005), Further study on two-thickness method for simultaneous measurement of complex EM parameters based on open-ended coaxial

probe, in *Proceedings of European Microwave Conference, Paris, France, 4–6 October*, IEEE Press, Piscataway, N. J.

Collin, R. E. (1991), *Field Theory of Guided Waves*, 2nd ed., IEEE Press, Piscataway, N. J.

Courtney, C. C., and W. Motil (1999), One-port time-domain measurement of the approximate permittivity and permeability of materials, *IEEE Trans. Microwave Theory Tech.*, *47*(5), 551–555, doi:10.1109/22.763154.

Engen, G. F., and C. A. Hoer (1979), Thru-Reflect-Line: An improved technique for calibrating the dual six-port automatic network analyzer, *IEEE Trans. Microwave Theory Tech.*, *27*(12), 987–998, doi:10.1109/TMTT.1979.1129778.

Hanson, G. W., and A. B. Yakovlev (2001), *Operator Theory for Electromagnetics: An Introduction*, Springer, New York.

Huber, C., H. Abiri, S. I. Ganchev, and R. Zoughi (1997), Modeling of surface hairline-crack detection in metals under coatings using an open-ended rectangular waveguide, *IEEE Trans. Microwave Theory Tech.*, *45*(11), 2049–2057, doi:10.1109/22.644234.

Hyde, M. W., and M. J. Havrilla (2008), A nondestructive technique for determining complex permittivity and permeability of magnetic sheet materials using two flanged rectangular waveguides, *Prog. Electromagn. Res.*, *79*, 367–386, doi:10.2528/PIER07102405.

Kwok, Y. K. (2002), *Applied Complex Variables for Scientists and Engineers*, Cambridge Univ. Press, Cambridge, U. K.

Li, C., and K. Chen (1995), Determination of electromagnetic properties of materials using flanged open-ended coaxial probe—Full wave analysis, *IEEE Trans. Instrum. Meas.*, *44*(1), 19–27, doi:10.1109/19.368108.

Maode, N., S. Yong, Y. Jinkui, F. Chenpeng, and X. Deming (1999), An improved open-ended waveguide measurement technique on parameters ε_r and μ_r of high-loss materials, *IEEE Trans. Instrum. Meas.*, *47*(2), 476–481, doi:10.1109/19.744194.

Mazlumi, F., S. Sadeghi, and R. Moini (2006), Interaction of rectangular open-ended waveguides with surface tilted long cracks in metals, *IEEE Trans. Instrum. Meas.*, *55*(6), 2191–2197, doi:10.1109/TIM.2006.884282.

Nicolson, A. M., and G. F. Ross (1970), Measurement of the intrinsic properties of materials by time-domain techniques, *IEEE Trans. Instrum. Meas.*, *19*(4), 377–382, doi:10.1109/TIM.1970.4313932.

Peterson, A. F., S. L. Ray, and R. Mittra (1998), *Computational Methods for Electromagnetics*, IEEE Press, Piscataway, N. J.

Popovic, D., L. McCartney, C. Beasley, M. Lazebnik, M. Okoniewski, S. C. Hagness, and J. H. Booske (2005), Precision open-ended coaxial probes for in vivo and ex vivo dielectric spectroscopy of biological tissues at microwave frequencies, *IEEE Trans. Microwave Theory Tech.*, *53*(5), 1713–1722, doi:10.1109/TMTT.2005.847111.

Richmond, J. H., and T. E. Tice (1955), Probes for microwave near-field measurements, *IRE Trans. Microwave Theor. Tech.*, *3*(3), 32–34, doi:10.1109/TMTT.1955.1124939.

Shin, D. H., and H. J. Eom (2003), Estimation of dielectric slab permittivity using a flared coaxial line, *Radio Sci.*, *38*(2), 1034, doi:10.1029/2002RS002776.

Stewart, J. W., and M. J. Havrilla (2006), Electromagnetic characterization of a magnetic material using an open-ended waveguide probe and a rigorous full-wave multimode model, *J. Electromagn. Waves Appl.*, *20*(14), 2037–2052, doi:10.1163/156939306779322693.

Stewart, J.W., and M. J. Havrilla (2007), A novel method for simultaneously extracting electric and magnetic properties of shielding materials using two coupled collinear open-ended waveguides, in *Proceedings of 23rd Annual Review of Progress in Applied Computational Electromagnetics, Verona, Italy, 19–23 March*, Appl. Comput. Electromagn. Soc., Monterey, Calif.

Tantot, O., M. Chatard-Moulin, and P. Guillon (1997), Measurement of complex permittivity and permeability and thickness of multilayered medium by an open-ended waveguide method, *IEEE Trans. Instrum. Meas.*, *46*(2), 519–522, doi:10.1109/19.571900.

Teodoridis, V., T. Sphicopoulos, and F. E. Gardiol (1985), The reflection from an open-ended rectangular waveguide terminated by a layered dielectric medium, *IEEE Trans. Microwave Theory Tech.*, *33*(5), 359–366, doi:10.1109/TMTT.1985.1133006.

Wang, S., M. Niu, and D. Xu (1998), A frequency-varying method for simultaneous measurement of complex permittivity and permeability with an open-ended coaxial probe, *IEEE Trans. Microwave Theory Tech.*, *46*(12), 2145–2147, doi:10.1109/22.739296.

Weir, W. B. (1974), Automatic measurement of complex dielectric constant and permeability at microwave frequencies, *Proc. IEEE*, *62*(1), 33–36, doi:10.1109/PROC.1974.9382.

Yeh, C., and R. Zoughi (1994), A novel microwave method for detection of long surface cracks in metals, *IEEE Trans. Instrum. Meas.*, *43*(5), 719–725, doi:10.1109/19.328896.

W. P. Baker, Department of Mathematics, Air Force Institute of Technology, Wright-Patterson AFB, OH 45433-7765, USA.

M. J. Havrilla, M. W. Hyde IV, and J. W. Stewart, Department of Electrical and Computer Engineering, Air Force Institute of Technology, Wright-Patterson AFB, OH 45433-7765, USA. (mhyde5@woh.rr.com)

D. P. Nyquist and E. J. Rothwell, Department of Electrical and Computer Engineering, Michigan State University, East Lansing, MI 48824-1226, USA.